Int. J. Renew. Energy Dev. 2025, 14 (2), 381-391

Contents list available at CBIORE journal website

International Journal of Renewable Energy Development

Journal homepage: https://ijred.cbiore.id

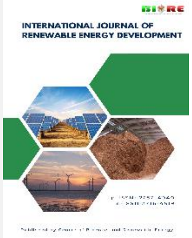

Research Article

Combined study to explore planar-mixed dimensional $Cs_3Bi_2I_9$ solar cells

Wan Zulhafizhazuan, Md Khan Sobayel Bin Rafiq, Shafidah Shafian, Suhaila Sepeai, Mohd Adib Ibrahim*

Solar Energy Research Institute (SERI), Level G Research Complex, Universiti Kebangsaan Malaysia, 43600 Bangi, Selangor, Malaysia

Abstract. The development of high-efficiency solar cells is of paramount importance for advancing sustainable energy technologies and meeting global energy demands. This study focuses on the optoelectronic performance of FTO/TiO_2/$Cs_3Bi_2I_9$/Spiro-OMeATAD/Ag planar heterojunction solar cells. Through detailed analysis, we investigated various factors such as crystallite size, strain, dislocation density, and their collective influence on the overall performance of the solar cells. Among the fabricated samples, sample A3 exhibited a significant improvement in efficiency, showing a 0.72% enhancement over the others. This increase is attributed to A3's superior crystallite quality, which led to reduced strain and a lower density of dislocations. These properties contribute to minimizing non-radiative recombination losses and enhancing charge carrier mobility, both of which are crucial for maximizing the photovoltaic performance of the device. These factors bring A3 closer to the theoretical Shockley-Queisser (S-Q) efficiency limit, a benchmark for photovoltaic performance. Further analysis using SCAPS-1D simulations supported these experimental findings, demonstrating the significance of optimizing critical parameters such as the minority carrier lifetime. The simulations revealed that high losses in short-circuit current density (J_{SC}) were a primary limiting factor in performance, emphasizing the need for careful tuning of these parameters to reduce losses. This work highlights the critical role of precise material engineering in developing highly efficient perovskite solar cells. The study not only provides insights into the structural and electronic properties essential for performance enhancement but also underscores the potential of $Cs_3Bi_2I_9$ as a promising material for photovoltaic applications. The findings offer valuable guidance for the next generation of high-efficiency, low-toxicity, and lead-free perovskite solar cells, aligning with global efforts to transition to clean, renewable energy sources.

Keywords: Solar cells, $Cs_3Bi_2I_9$, optoelectronic properties, Shockley-Queisser limit, material engineering

Received: 11th Sept 2024; Revised: 27th Dec 2024; Accepted: 15th Feb 2025; Available online: 28th Feb 2025

1. Introduction

The global energy landscape remains critically dependent on fossil fuels, which are primary contributors to environmental degradation. The extensive use of coal, oil, and natural gas has resulted in significant pollution, accelerating climate change and causing widespread health issues (Thomas O.,2024). The dual challenge of meeting increasing energy demands while mitigating environmental damage underscores the urgent need to transition to sustainable, energy efficient and renewable energy sources (Basher *et al.*, 2021) (Iftekharuzzaman *et al.*, 2023) (Nur-E-Alam *et al.*, 2024). Solar energy, characterized by its cleanliness, abundance, and inexhaustibility, has emerged as a pivotal solution to reducing our dependence on fossil fuels.

In the pursuit of more efficient solar energy harnessing, perovskite solar cells (PSCs) have made significant strides in the field of photovoltaics (NREL, 2024). These cells have demonstrated substantial improvements in efficiency and cost-effectiveness, positioning them as a promising candidate for large-scale solar energy deployment (Razza *et al.*, 2016). However, the widespread adoption of PSCs is impeded by their reliance on lead-based materials, which pose severe risks to both human health and the environment. Lead, a highly toxic heavy metal, not only endangers health but also raises concerns regarding environmental safety, particularly as these materials degrade over time (Yu *et al.*, 2022). A different study shows that the separation of diffraction peaks, specifically at (312) and (411), suggests an increase in lattice distortion and micro-strain within the material. This peak dissociation serves as evidence of the structural expansion and confirms the degradation or breakdown of the perovskite films (Nur-E-Alam, Islam, *et al.*, 2024).Additionally, the instability of lead-based perovskites, which are prone to degradation under environmental conditions, further complicates their commercialization.

To address the challenges of toxicity and instability in lead-based PSCs, researchers are actively exploring lead-free alternatives (Mosabbir *et al.*, 2024) . Among these, cesium bismuth iodide ($Cs_3Bi_2I_9$) has emerged as a particularly promising candidate (Waykar *et al.*, 2020). $Cs_3Bi_2I_9$ holds the potential to retain many of the beneficial properties of traditional perovskites, such as cost-effective fabrication, without the associated lead toxicity. The development of $Cs_3Bi_2I_9$-based solar cells represents a crucial step towards achieving environmentally sustainable and stable perovskite

---

* Corresponding author
Email: mdadib@ukm.edu.my (M. A. Ibrahim)

https://doi.org/10.61435/ijred.2025.60642
ISSN: 2252-4940/© 2025.The Author(s). Published by CBIORE

solar technology, in line with global efforts to reduce hazardous materials in renewable energy technologies (Johansson *et al.*, 2019).

Understanding the working mechanism of perovskite solar cells is essential for appreciating their potential and guiding future innovations. Perovskite materials are defined by their unique crystal structure, which facilitates efficient light absorption and charge generation (Mohamad Noh *et al.*, 2018). In a perovskite solar cell, the perovskite layer absorbs sunlight, generating excitons (bound electron-hole pairs), which are subsequently separated into free carriers. These carriers are transported through the cell via the electron transport layer (ETL) and the hole transport layer (HTL), both of which are critical for efficient charge extraction and minimizing recombination losses (Namatame *et al.*, 2017) (Max-Planck-Gesellschaft, 2024.) (Debbie C, 2024). The quality of $Cs_3Bi_2I_9$ also needs to be prioritized to enhance performance.

The efficiency of a solar cell is largely determined by the quality of its absorber layer, responsible for capturing sunlight and converting it into electricity. Key factors influencing this layer's quality include the material's band gap, absorption coefficient, the mobility and lifetime of charge carriers, all of which are vital for effective sunlight-to-electricity conversion (O *et al.*, 2016). The crystalline structure, thickness, and presence of defects in the absorber layer also significantly impact efficiency, with better crystallinity and fewer defects leading to higher performance (Ahamd *et al.*, 2020). Moreover, the methods used for depositing the absorber layer and subsequent post-treatment processes, such as annealing, can further improve its structural properties and reduce defects (Liou *et al.*, 2014).

Recent research has focused on improving the performance of Bi-based perovskite solar cells, with promising outcomes indicating advancements in both efficiency and stability (Hamukwaya *et al.*, 2022) (Zhang *et al.*, 2019) (Johansson *et al.*, 2016). Various strategies have been explored to optimize the material's properties, including modifications to the crystal structure, enhancements in the interface between layers, and the development of more effective ETL and HTL materials (Rai *et al.*, 2020) (Yin *et al.*, 2019) (M. B. Islam *et al.*, 2017) (Li *et al.*, 2021) (Lian *et al.*, 2018; Mohamad Noh *et al.*, 2018). The progress made in $Cs_3Bi_2I_9$ research underscores its potential to become a leading material in the development of lead-free perovskite solar cells, offering a safer and more sustainable alternative to lead-based technologies. This paper examines the latest advancements in $Cs_3Bi_2I_9$ perovskite solar cells, exploring their working principles and the cutting-edge research driving their development towards commercial viability.

Despite these advancements, the power conversion efficiency (PCE) of $Cs_3Bi_2I_9$ solar cells remains lower than that of lead-based perovskites, primarily due to its indirect band gap and suboptimal charge transport properties (Ghosh *et al.*, 2018), which are exacerbated by inadequate optimization of CsI concentration during synthesis. With a band gap of approximately 2.2 eV, $Cs_3Bi_2I_9$ is ideally suited for efficient solar energy conversion for tandem application. While strategies such as bromine alloying have been explored to address this issue, the critical role of CsI concentration on the band gap and overall material performance has not been sufficiently investigated. Variations in CsI concentration can significantly alter the crystal structure, impacting both charge transport and material stability. However, systematic studies on these effects are still lacking. A comprehensive approach that combines simulation studies using SCAPS-1D software, along with film optoelectronic analysis and device fabrication, could provide valuable insights into optimizing $Cs_3Bi_2I_9$ for solar cell applications. This research could reveal how varying CsI levels can enhance the material's structural, optical, and electronic properties, ultimately improving its photovoltaic performance and long-term stability.

2. Materials

2.1 Materials and Film Growth

The materials used in this study included high-purity chemicals and specialized substrates to ensure optimal results. bismuth iodide (BiI_3, 99 %) and cesium iodide (CsI, 99.9 %) were sourced from Sigma-Aldrich. N,N-dimethylformamide (DMF, anhydrous, 99.8 %) and methanol (CH_3OH, anhydrous, 99.8 %) were also obtained from Sigma-Aldrich, along with titanium diisopropoxide bis(acetylacetonate) (75 % in isopropanol) for the preparation of the TiO_2 precursor solution. Fluorine-doped tin oxide (FTO) conducting glass with a sheet resistance of less than 15 Ω/square (Pilkington TEC 15, 15 Ω^{-1}) served as the substrate. Cleaning agents such as detergent, acetone, and hydrochloric acid (HCl, 2 M) were employed in the substrate preparation process. Zinc powder and spiro-OMeTAD were utilized for subsequent layers, with spiro-OMeTAD dissolved in chlorobenzene. Dopants included lithium bis(trifluoromethanesulfonyl)imide (LiTFSI) and tert-butylpyridine (TBP) to enhance conductivity and performance. A 0.15 M solution of titanium diisopropoxide bis(acetylacetonate) was specifically prepared for TiO_2 layer formation. All materials were handled with precision to ensure the integrity and reproducibility of the experimental results.

2.2 Developed Thin Film Characterization

Characterization of the samples was performed using several advanced techniques. X-ray diffraction (XRD) patterns of the perovskite films were obtained with a BRUKER D8 ADVANCE system, utilizing CuKα radiation (λ = 1.5405 Å) at ambient conditions and room temperature. Field emission scanning electron microscopy (FE-SEM) was conducted using a Carl Zeiss Merlin model, operating in high vacuum and high-resolution mode with an integrated high-efficiency in-lens detector, to analyse the topography and elemental composition. The absorption spectrum was analysed using a PerkinElmer Lambda 950 spectrophotometer. Photoluminescence (PL) and time-resolved photoluminescence (TRPL) measurements were performed using an Edinburgh Instruments FLS920 model, equipped with a 450 W xenon lamp as the excitation source and double grating excitation and emission monochromators. All optical measurements were carried out at room temperature on thin films deposited on glass substrates, with PL emission spectra recorded using an excitation wavelength of 375 nm. The light current-voltage (LIV) characteristic curves of the fabricated perovskite solar cells (PSCs) were measured under standard AM 1.5 sunlight (100 mW/cm²) using an Interface 1010 system from Gamry with a Xenon light source. The effective area of the cell was defined as 0.07 cm² using a non-reflective metal mask.

3. Methodology

In this experiment, a three-step approach was undertaken. First, the study focused on investigating the effects of varying molar ratios in $Cs_3Bi_2I_9$ perovskite films. Second, solar cells were fabricated using the perovskite films studied in the first step. Finally, simulations were performed using SCAPS-1D, incorporating experimental data to model real-world device, followed by an optimization process aimed at achieving higher efficiency.

3.1 Optoelectronic Investigation

SLG substrates were cleaned with a detergent, followed by distilled water, acetone, methanol, IPA and deionised water for 10 min for each solvent, and blow dry with nitrogen gas. And finally, substrates were heated for 10 min at 120°C. BiI_3 precursor was dissolve in DMF 0.343 M and five different molarity of CsI was dissolved in DMF (0.515, 0.615 and 0.715M). As the solute fully dissolved, the precursor was mixed with CsI and labelled according to mole ratio CsI to BiI_3 as A1(1.501:1), A2(1.79:1) and A3(2.084:1). Mixed solutions were stirred on a hot plate at 70°C for overnight to prepare an orange uniform solution. $Cs_3Bi_2I_9$ thin film was deposited on a clean SLG substrate by placing the substrate on a spin-coater and setting the program at 5000 rpm for 20 s. Then 40 µl of the prepared solution $Cs_3Bi_2I_9$ was dropped on the substrate using a micropipette, and spin-coated at 5000 rpm for 20 s. The deposited thin films were annealed at 100°C for 30 min. The experimental procedure is shown in Figure 1.

For XRD analysis, the crystallite size (D) was then calculated using the Scherrer formula, shown in Equation 1. Here, D represents the crystallite size, λ is the wavelength, θ is the diffraction angle, β is the FWHM, and k is the Scherrer constant (k = 0.9). The micro-strain was calculated using Equation 2, and the dislocation density using Equation 3.

$$D = \frac{k\,\lambda}{\beta\ \mathrm{Cos}\theta} \tag{1}$$

$$\varepsilon = \frac{\beta}{4tan\theta} \tag{2}$$

$$\delta = \frac{1}{D^2} \tag{3}$$

Bragg's Law is a key principle in X-ray diffraction that explains how X-rays interact with the atomic planes in a crystal. The law is expressed by the Equation (4). λ is the wavelength of the incident X-rays, d is interplanar spacing, and θ is the angle of incidence, which is the angle between the incoming X-rays and the crystal planes. Bragg's Law is fundamental in determining the crystal structure by analysing the angles at which X-rays are scattered, providing insights into the spacing between atomic planes within the crystal. This relationship allows scientists to deduce structural information about the crystal based on the diffraction patterns observed when X-rays are directed at the material (Bragg H.W., B.L.W.,1913).

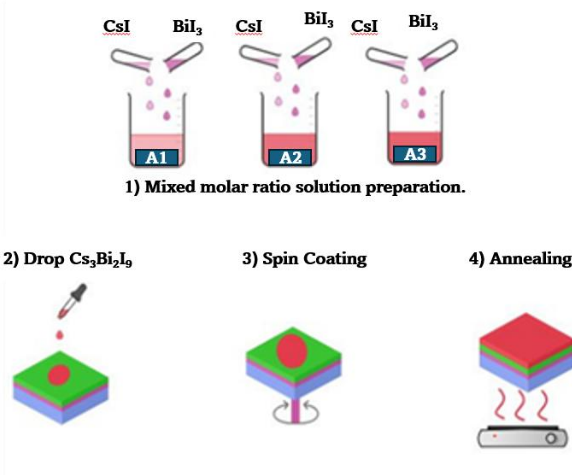

Fig 1. Solution preparation and $Cs_3Bi_2I_9$ film deposition experimental procedure.

$$n\lambda = 2d\ Sin\theta \tag{4}$$

In this study, the band gap was determined by plotting a graph between $(\alpha hv)^2$ and $(hv)^2$, where the extrapolation of the straight line to $(\alpha hv)^2 = 0$ provides the energy band gap value. The bandgap was calculated using Equation 5. Where, α = absorption coefficient, Eg = band gap of the material, A = constant, hv = Energy of the incident photon (eV), n = nature of transition (n = 2 and 1 = 2 for direct and indirect bandgap respectively). However, direct and indirect bandgap differs based on the emission of a photon. As in the case of an indirect bandgap, the photon was passed through the intermediate state and did not emit directly and transfer the momentum of a crystal lattice, whereas, in the case of a direct bandgap transition, the emission of a photon is direct due to the identical momentum of hole and electron in the conduction band and valence band. Although, the absorption coefficient (α) can be calculated using the Lambert-Beer law as in Equation 6. Where A=absorbance of material, t=thickness.

$$(\alpha hv)^{\frac{1}{n}} = \mathrm{A}(hv - E_g) \tag{5}$$

$$I = I_O e^{-\alpha t,} (\alpha = 2.303.\mathrm{A/t}) \tag{6}$$

3.2 $Cs_3Bi_2I_9$ perovskite solar cell fabrication

The FTO substrates were meticulously cleaned using a series of solvents: detergent, distilled water, acetone, methanol, IPA, and deionized water, each for 10 min, followed by nitrogen gas blow-drying. Subsequently, the substrates were heated at 120 °C for 10 min. A TiO_2 precursor solution was prepared by dissolving titanium diisopropoxide bis(75% acetylacetone) in 1 ml of 1-butanol. This solution was spin-coated onto the substrates at 3500 rpm for 30 seconds. The coated substrates were then preheated on a hot plate at 120°C for 5 min to evaporate the solvent and initiate TiO_2 layer formation, a process repeated twice. Next, the substrates were calcined in a furnace at 500 °C, with a temperature ramping rate of 18°C/min, to crystallize the TiO_2 and enhance its compactness. After gradual cooling to room temperature, the substrates were inspected for uniformity and defects. The subsequent deposition of $Cs_3Bi_2I_9$ film on the substrate is detailed in the film deposition experimental study section. For the spiro-OMeTAD deposition, a solution was prepared by dissolving 61.3 mg of spiro-OMeTAD powder in 1 ml of chlorobenzene, supplemented with 17.5 µL of lithium bis(trifluoromethanesulfonyl)imide (Li-TFSI) and 28.8 µL of 4-tert-butylpyridine (tBP) to enhance conductivity and performance. This solution was spin-coated onto the substrates at 4000 rpm for 20 seconds to ensure a uniform layer. The coated substrates were then allowed to sit in ambient air to facilitate oxidation for overnight. Post-oxidation, the substrates were inspected for uniformity and defects, ensuring the Spiro-OMeTAD layer was smooth and homogeneous. Finally, Ag electrode was grown at 70 nm thickness by using vacuum thermal evaporator. Overall procedures were illustrated as in Figure 2.

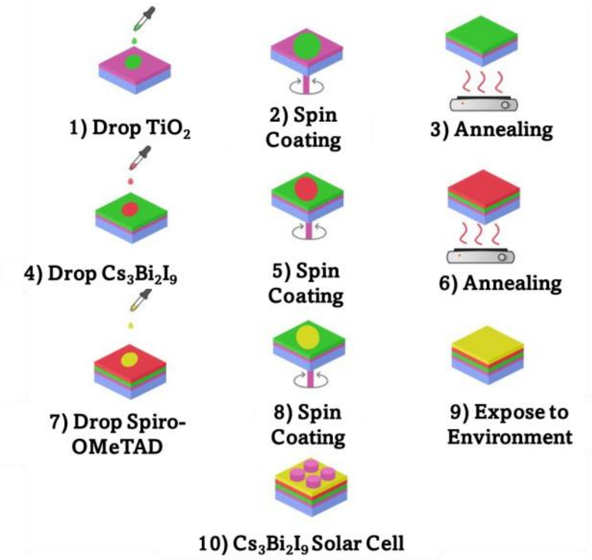

Fig 2. $Cs_3Bi_2I_9$ perovskite solar cell fabrication process.

Besides the performance of the solar cell, a key parameter to consider is the carrier lifetime, which represents the average time an electron or hole exists before recombining. Carrier lifetime by Equation 7 plays a crucial role in determining the diffusion length, a factor that directly influences charge collection efficiency. Here, L_{DIFF} is the diffusion length, τ is the carrier lifetime, and D is the diffusion coefficient. A longer carrier lifetime increases diffusion length, allowing carriers to travel farther before recombining. The diffusion coefficient (D) for charge carriers in a semiconductor is linked to the carrier mobility (μ) and the thermal voltage (V_T) through the Einstein relation as in Equation 8. Here, the mobility represents how easily carriers move in response to an electric field, and the thermal voltage depends on the temperature (T) and fundamental constants such as the Boltzmann constant (k_B) and the charge of the carrier (q). This equation indicates that the diffusion coefficient is directly proportional to both the carrier mobility and the thermal energy, making it a crucial factor in determining how charge carriers spread out in a semiconductor material.

$$L_{DIFF}= \sqrt{(\tau * D)} \qquad (7)$$

$$D = \mu(V_T/q), \text{ where } (V_T = k_B T) \qquad (8)$$

3.3 Simulation fabricated device and its optimization

SCAPS (Solar Cell Capacitance Simulator) is a one-dimensional solar cell simulation programme developed at the Department of Electronics and Information Systems (ELIS) of the University of Gent, Belgium. SCAPS can be used as a resource to validate the characteristics and performance of all types of solar cell. SCAPS-1D software works on two basic equations, that are the Poisson equation and the continuity equation of electrons and holes in steady state manner which are expressed in Equation 9, 10 and 11. The Poisson equation is as follow:

$$\frac{d^2}{dx^2}\psi(x) = \frac{e}{\varepsilon_0 \varepsilon_r}\left(p(x) - n(x) + N_D - N_A + \rho_p - \rho_n\right) \qquad (9)$$

Here, ψ is electrostatic potential, N_D and N_A are donor and acceptor concentrations, e is electrical charge, ε_r is relative permittivity and ε_0 is the vacuum permittivity, ρ_p and ρ_n are holes and electrons distribution, respectively. The continuity equations for electrons and holes are as following:

$$\frac{dJ_n}{dx} = G - R \qquad (10)$$

$$\frac{dJ_p}{dx} = G - R \qquad (11)$$

In this study, we use SCAPS-1D (Solar Cell Capacitance Simulator in One Dimension) to optimize solar cell performance

Table 1
Simulation parameters as gain from experimental.

Parameter	Spiro-OMeATAD	$Cs_3Bi_2I_9$	TiO_2	FTO
Thickness (nm)	20	1000	40	580
Bandgap (eV)	3.06	2	3.26	3.5
Electron affinity (eV)	2.05	3.4	4.2	4
Dielectric permittivity (relative)	3	9.68	10	9
CB effective density of states (cm^{-3})	2.8 X 10^{19}	1 X 10^{19}	2.42 X 10^{18}	1 X 10^{19}
VB effective density of states (cm^{-3})	1 X 10^{19}	2.1 X 10^{19}	1.8 X 10^{19}	1 X 10^{18}
Electron mobility (cm^2 /Vs)	2 X 10^{-4}	4.3	3.5 X 10^{2}	1 X 10^{7}
Hole mobility (cm^2 /Vs)	2 X 10^{-4}	1.7	2	1 X 10^{7}
Donor concentration (cm^{-3})	0	1 X 10^{14}	1 X 10^{18}	1 X 10^{19}
Acceptor concentration (cm^{-3})	1 X 10^{18}	1 X 10^{14}	0	1 X 10^{15}
Temperature (K)		300		
Bulk defect density (cm^{-1})		1 X 10^{14}		
$Cs_3Bi_2I_9$/NiO defect density (cm^{-1})		1 X 10^{10}		
$Cs_3Bi_2I_9$/TiO_2 defect density (cm^{-1}))		1 X 10^{10}		

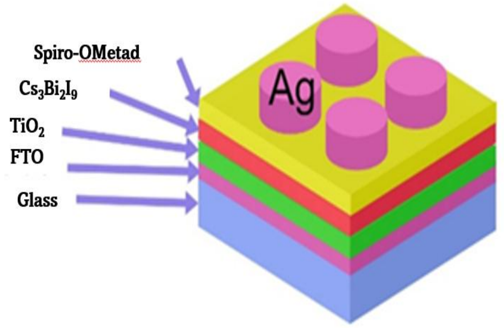

Fig 3. Solar cell model in SCAPS-1D simulation software.

with the configuration FTO/ TiO_2/$Cs_3Bi_2I_9$/Spiro-OmeAtad/Ag, aiming to achieve the theoretical S-Q limit started with model same as fabricated solar cell. The process begins by defining the material properties of the solar cell layers, including bandgap energy, carrier concentration, and carrier mobilities based on experimental data. We configure the device structure in SCAPS-1D, specifying the thickness and doping concentration for each layer as in Figure 3. Key solar cell parameters such as optical constants, defect densities, and interface properties are input into the simulator for accurate device characterization. The simulation environment is set up with an AM1.5G spectrum, a temperature of 300 K, and fixed incident illumination intensity. Initial simulations provide baseline efficiency metrics, including J-V curves and power conversion efficiency. We systematically vary key parameters, such as absorber thickness and bulk defect densities, to observe their impact on efficiency, utilizing SCAPS-1D's optimization tools to maximize performance by reducing recombination and enhancing carrier collection. We compare the optimized model's performance, as shown in Table 1, with the theoretical S-Q limit to evaluate the proximity to ideal performance, identifying loss mechanisms through detailed analysis of the device architecture. This iterative process involves refining parameters based on previous results, validating simulation outcomes against the S-Q limit, and understanding the energy losses in the device. This methodology offers a comprehensive approach to deeply understanding and optimizing solar cells using SCAPS-1D, striving to closely approach or achieve the S-Q limit.

4. Results and discussion

4.1 Analysis of $Cs_3Bi_2I_9$ Films.

4.1.1 Structure analysis.

XRD is a widely used technique for analysing the structure and crystalline properties of materials. The XRD spectra for all samples are presented in Figure 4 and were analysed using Diffrac.eva to confirm the phase and extract key parameters such as wavelength, diffraction angle, and full width at half maximum (FWHM). The crystallite size (D) was determined using the Scherrer formula stated as Equation 1, with micro-strain and dislocation density calculated using Equations 2 and 3, respectively. In this study, XRD analysis was applied to examine the crystallographic properties, including crystallinity and crystal phases, of the prepared $Cs_3Bi_2I_9$ film, as shown in Figure 4(a). The phases $Cs_3Bi_2I_9$ and $Cs_3(I_3(BiI_3)_2)$ were identified by matching them with the patterns PDF01-089-1846 ($Cs_3Bi_2I_9$) and PDF01-070-0666 ($Cs_3(I_3(BiI_3)_2)$). Despite differences in their chemical nomenclature, both phases exhibited identical lattice properties, including a hexagonal structure with space group P6(3) / mmc (194), lattice parameters a = b = 8.404 Å, c = 21.183 Å, and a volume of 1300.87 Å^3. These characteristics confirm the formation of a crystal structure typical of $A_3B_2X_9$ perovskite derivatives.

The relationship between FWHM variations in Figure 4(b) and crystallite size is well-established in materials science, particularly through XRD studies. Smaller FWHM values indicate larger crystallite sizes because narrower XRD peaks suggest fewer defects and lower strain in the crystal lattice, resulting in larger coherent scattering domains (M. A. Islam *et al.*, 2020). This inverse relationship is consistent with our findings, where A3 displayed the largest crystallite size due to its smallest FWHM value as in Figure 4(c). The correlation between crystallite micro-strain and size is also important as shown in Figure 4(d), as higher micro-strain generally corresponds to smaller crystallite sizes (Akhtaruzzaman *et al.*, 2021). This observation is supported by other research, showing that preparation conditions such as deposition and annealing significantly affect both crystallite size and strain levels. These findings, along with the correlation between FWHM and crystallite size as derived from the Scherrer equation, reinforce the understanding that crystallite size and micro-strain are closely linked. The preparation conditions play a critical role in determining these characteristics, with observed trends in FWHM and crystallite size offering valuable insights into the structural properties of the materials studied.

Crystallite size is particularly important in perovskite materials, influencing ion migration and device stability. For example, in perovskite films like $MAPbBr_3$, variations in grain size can significantly affect the activation energy required for ion migration, which is key to the long-term stability of perovskite solar cells (McGovern *et al.*, 2021). Research indicates that larger grain sizes, achieved by adjusting spin-coating times, can

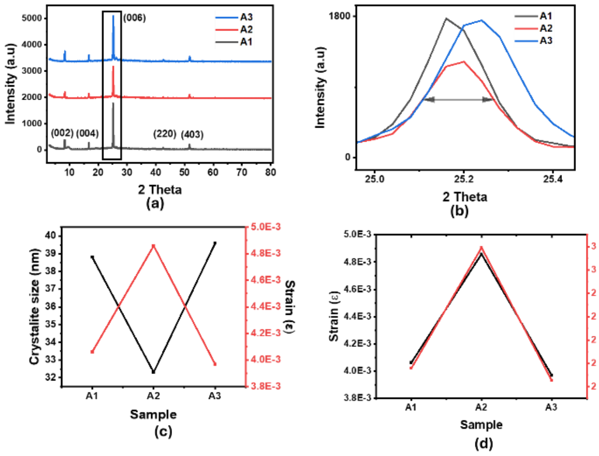

Fig 4. (a) XRD spectra highlighting the effects of varying stoichiometric mix ratios. (b) FWHM changes due to the mix ratio. (c) The influence of mix ratio adjustments on crystallite size and strain (d) The correlation between mix ratio variations, strain, and dislocation density.

reduce ion migration by altering the pathways ions take through the material. Studies have shown that grain sizes between 2 to 11 μm can help mitigate ion migration, which is often more pronounced at grain boundaries. Additionally, the crystallite size of perovskite layers directly influences lattice strain and overall crystal structure. This relationship highlights the importance of optimizing crystallite size to improve performance in optoelectronic devices by minimizing defects and improving charge transport. The interplay between crystallite size, lattice strain, and ion migration underscores the necessity of careful material engineering to enhance the efficiency and stability of perovskite-based devices.

4.1.2 Compositional and morphological analysis

The SEM images (A1 to A3) in Figure 5 reveal a clear progression in particle density and morphology. In Figure 5(a), the particles are sparse and irregularly shaped, scattered unevenly across the surface. In Figure 5(b), while the particle density remains low, the shapes become more varied, including both spherical and elongated forms. By Figure 5(c), the particles have mostly become spherical and are more closely packed, indicating an increase in density. This progression from A1 to A3 suggests a trend toward higher particle density and uniformity, indicating that the film exhibits mixed particle dimensionality. The presence of mixed particle shape within a single perovskite film can be viewed as a form of heterojunction. The interfaces between perovskite structures of different shape particle create regions with distinct electronic properties (Zhou *et al.*, 2023). These internal heterojunctions function similarly to traditional heterojunctions, offering advantages in optoelectronic applications by enhancing charge separation, reducing recombination rates, and improving overall device efficiency.

Table 2 shows the elemental composition of $Cs_3Bi_2I_9$ films, revealing an inverse relationship between iodide and cesium percentages across the samples. Sample A1 has the highest iodide content at 58.5% and cesium content at 20%. In contrast, Sample A3 has the lowest iodide content at 51.6% and the highest cesium content at 22.7%. The bismuth content varies independently, with sample A2 having the lowest at 17.3%, highlighting distinct compositional differences across the samples. Interestingly, the CsI concentration data shows an unexpected trend: the concentration in the film does not consistently increase with the molarity of CsI. By data integration from Table 2 and Figure 6(b), it becomes clear that the CsI concentration in the film is closely related to the interplanar distance in the lattice. As the interplanar distance increases, the CsI percentage decreases. This is because tensile strain limits the number of Cs atoms that can bind with Bi and I atoms during the formation of the $Cs_3Bi_2I_9$ lattice (Han *et al.*, 2019). Since the Cs atom has a larger radius, its binding energy is more easily affected by the presence of tensile strain in the film. Similarly, during orbital overlapping, an increase in planar distance indirectly reduces the number of overlapped orbitals, which in turn reduces the binding energy needed to form the film. Because Cs has the lowest electronegativity, it is harder to bind and form the lattice under these conditions. Interplanar distance can be calculated by using Equation 4. Value for the peak shift is shown at Figure 6(a).

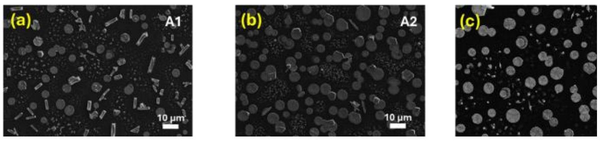

Fig 5. FESEM image illustrating the impact of varying precursor mix ratios.

Table 2
Compositional analysis of $Cs_3Bi_2I_9$

Sample	Iodide (%)	Cs (%)	Bi (%)
A1	58.5	20.0	21.5
A2	57.2	17.3	25.5
A3	51.6	22.7	25.7

4.1.3 Electrical analysis

The analysis of mobility and resistance across three samples with different mix molar ratios highlights a clear relationship with interplanar distance as shown in Figure 6. Figure 6(a) shows a peak shift at 12.84°, which reflects a change in the interplanar distance of the sample. This correlation is further illustrated in Figure 6(b), where the peak shift is coherently linked to variations in the interplanar spacing. Interplanar distance, which is the spacing between atomic planes in a crystal lattice, has a direct impact on the material's electrical properties (Hartono *et al.*, 2019). When the interplanar distance is smaller, atoms are more closely packed, leading to better overlap of atomic orbitals. This scenario typically increases the mobility of charge carriers, allowing them to move more easily through the material, which in turn lowers resistance as shown Figure 6(c). On the other hand, a larger interplanar distance suggests a more relaxed lattice structure, which can hinder the movement of charge carriers, resulting in reduced mobility and higher resistance.

The molar ratio of the components in each sample plays a crucial role in determining the interplanar distance, and thus affects mobility and resistance. For example, Sample A3, with the highest molar ratio, likely has the smallest shift of interplanar distance, leading to the highest mobility and lowest resistance. Sample A2, with an intermediate molar ratio, may have a largest shift of interplanar distance, resulting in lowest mobility and highest resistance. Sample A1, with the lowest molar ratio, likely exhibits the moderate interplanar distance shift, which corresponds to the moderate mobility and resistance among the samples. Therefore, adjusting the molar ratio to achieve the optimal interplanar distance is key to fine-tuning the electrical properties of these materials for specific applications.

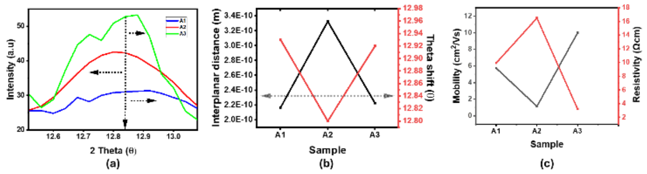

Fig 6. (a) A peak shift observed at 12.84 due to changes in the molar mix ratio. (b) The relationship between interplanar distance and peak shift as the mix ratio varies (c) The correlation between mix ratio variations, mobility, and resistance.

4.1.4 Optical analysis

The absorbance spectra of $Cs_3Bi_2I_9$ thin films prepared under different mix ratio (A1, A2, and A3) were measured across a wavelength range of 300 to 1100 nm to investigate their optical properties, as shown in Figure 7(a). In the UV region (300-400 nm), all samples exhibited a significant decreased in absorbance as the wavelength decreased towards 300 nm, indicating strong UV light absorption. In the visible region (400-700 nm), most samples displayed notable absorption features around 450-500 nm, corresponding to the blue-green part of the spectrum, where strong electronic transitions typically occur. Specifically, in the 500-600 nm range, samples A1 and A2 showed a significant absorption peak around 550 nm, while sample A3 had a peak at 600 nm, indicating high absorbance in the green-yellow region. This characteristic is crucial for applications involving visible light harvesting, such as photovoltaic cells. Additionally, extended absorption was observed from 300 nm to 1100 nm.

The bandgap energies of the samples were determined using the Tauc plots method shown in Figure 7(b) (Bai *et al.*, 2018). Linear extrapolation of the curves indicated bandgap energies of 1.9 eV for A1, 2.1 eV for A2 and 2.0 eV A3. The variations in bandgap energies among the samples underscore the impact of compositional adjustments on the electronic properties of $Cs_3Bi_2I_9$, which is essential for optimizing its use in optoelectronic devices like solar cells. Figure 7(b) shows that sample A2 has the highest bandgap energy, while sample A1 has the lowest. The differences in bandgap values can be attributed to the hybridization that occurs at the orbital level during crystallite formation, which affects the optical band gap (Feierabend *et al.*, 2017) (Yao *et al.*, 2022). This is evident from the peak shift at 12.84, indicating the presence of lattice strain, which alters the interplanar distance as in Figure 6(b). For example, when the gap between the reference peak and the shifted peak is large and increases, the optical band gap also increases. Conversely, a smaller and reduced interplanar gap results in a lower bandgap. The presence of lattice strain in the film leads to these changes, as the increase in interplanar distance enhances atomic orbital overlap, while tensile strain increases the optical band gap by reducing orbital overlap. This phenomenon has been previously explained in relation to the impact of elemental composition on tensile strain formation. Figure 7(c) illustrates the signal intensity as a function of wavelength (500-800 nm) for three samples (A1 to A3). All samples show a general increase in intensity, peaking around 750 nm, followed by a decline. Among them, sample A3 exhibits the highest intensity across all wavelengths, while A1 and A2 display progressively lower intensities. The sharp peak at 750 nm is most pronounced in A1, indicating a higher concentration or unique property in this sample, suggesting it has high radiative recombination. As shown in Table 3, A3 also has a highest minority carrier lifetime compared to others. However, overall sample shows carrier lifetime still low since to high carrier lifetime require to fabricate high efficiency solar cell.

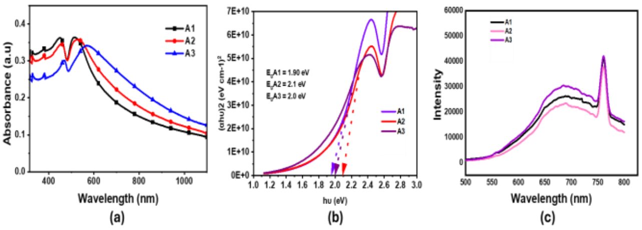

Fig 7(a) UV-vis absorption spectra of $Cs_3Bi_2I_9$ at different molar ratios. (b) Tauc plot used to determine the optical band gap. (c) Impact of different molar ratios on photoluminescence properties.

4.2 $Cs_3Bi_2I_9$ perovskite solar cell fabrication and Simulation

Table 4 provide the performance metrics for the fabricated $Cs_3Bi_2I_9$ solar cells. Among the tested samples, A3 exhibits the

Table 3
The effect of varying molar ratios on carrier minority lifetime.

Sample A	**A1**	**A2**	**A3**
B_1	0.1350	0.0640	0.0660
Std. Dev	0.0038	0.0035	0.0024
τ_1(ns)	0.0431	0.0385	0.0469
Std. Dev (ns)	0.0012	0.0021	0.0017
B_2	0.0000	0.0000	0.0000
Std. Dev	0.0000	0.0000	0.0000
τ_2(ns)	3.1320	47.6400	2.1855
Std. Dev (ns)	1.3560	31.8200	0.5740
B_3	0.0000	0.0000	0.0000
Std. Dev	1.6800	0.0000	0.0000
τ_3(ns)	9.1110	49.7300	35.6800
Std. Dev (ns)	8.7900	34.0000	26.0200
$\chi2$	1.7210	1.4660	1.3300
Average lifetime((ns)	**0.0431**	**0.0385**	**0.0469**

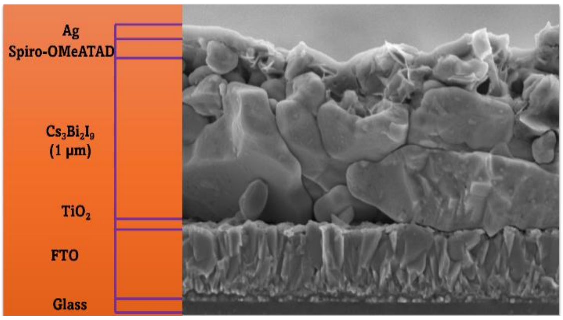

Fig 8. FESEM cross section image for A3 device.

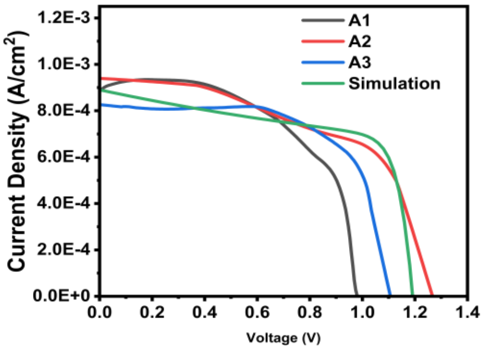

Fig 9. LIV fabricated and simulation of $Cs_3Bi_2I_9$ solar cell.

highest efficiency, improving by 0.72% due to its superior optoelectronic properties. This enhancement is primarily attributed to the larger crystallite size of A3, which leads to reduced recombination, as evidenced by the sample's low strain and dislocation density (Morales & Al-Shomar, 2024) (Sarkar *et al.*, 2022). Electrically, A3 demonstrates the highest carrier mobility and the lowest resistance, supported by a smaller interplanar distance that facilitates easier carrier movement within the lattice (Ng *et al.*, 2022). Additionally, A3 shows strong absorption and minimal non-radiative recombination losses. Its extended carrier lifetime further improves performance by enhancing the transfer of electron-hole pairs to the electrode (Cheng *et al.*, 2022) (Zhang *et al.*, 2022). On the other hand, sample A2 performs the worst, reflecting weaker optoelectronic properties that reduce efficiency. Overall, A3 shows a clear advantage with a 0.72% improvement in efficiency compared to the other samples.

The carrier lifetime, which measures the average time a charge carrier (electron or hole) exists before recombining, is a key factor influencing solar cell efficiency (Yun *et al.*, 2019; Jung *et al.*, 2019). It directly affects the diffusion length and the optimal thickness of the perovskite layer. Figure 8 illustrates the cross-sectional structure of the A3 device, which includes layers of Spiro-OMeTAD, $Cs_3Bi_2I_9$, TiO_2, FTO, and the substrate. As indicated by Equation 10, a longer carrier lifetime increases the diffusion length, allowing charge carriers to travel farther and reach the electrodes before recombining. For efficient charge collection, the semiconductor thickness should ideally be close to or less than the diffusion length (Aliaghayee, 2023; Yadav *et al.*, 2024). If the thickness exceeds the diffusion length, carriers generated deep within the material may recombine before reaching the junction, leading to lower device efficiency. As a result, the reduced carrier collection decreases the short-circuit current (J_{SC}), ultimately lowering overall device performance (Yadav *et al.*, 2024). Figure 8 also highlights the absorber layer thickness of approximately 1.1 µm, combined with a low carrier lifetime of about 0.046 ns, which contributes to the reduced current collection at the terminal.

When comparing the fabricated solar cells to the S-Q limit, the increase in open-circuit voltage (V_{OC}) follows the trend dictated by the optical bandgap (Rühle, 2016). Sample A2 exhibits the highest V_{OC} at 1.25V, which is consistent with its larger bandgap of 2.1 eV. In contrast, Sample A1 shows the lowest V_{OC} at 0.9 V, corresponding to a 1.9 eV bandgap. Despite these differences in Voc, all samples demonstrate lower overall efficiency compared to the S-Q limit, primarily due to reduced short-circuit current density (J_{SC}). Interestingly, the J_{SC} values are relatively consistent across all samples, suggesting that the variation in efficiency is driven by factors other than J_{SC} alone. Among the samples, Sample A3 stands out, showing a 0.72% improvement in efficiency compared to the others. This superior performance is attributed to the exceptional quality of its material, bringing it closer to the S-Q limit, as shown in Table 4.

In evaluating the performance of fabricated photovoltaic devices, it is crucial to understand the underlying mechanisms that contribute to losses within the system. SCAPS-1D (Solar Cell Capacitance Simulator in One Dimension) is a widely used simulation tool that enables researchers to model and predict the performance of solar cells by simulating various physical phenomena, including recombination losses, series resistance, and optical losses (Ahmed *et al.*, 2023) (Ramli *et al.*, 2017). By comparing the simulated outcomes with the actual performance of fabricated devices, we can identify discrepancies and areas for optimization. Relevant optoelectronic and physical parameter gained from experimental were used to simulate our fabricated solar cell as in Table 1. Via this method the losses in fabricated solar cells can be reflected by the optimization work by simulation.

Figure 9 presents the LIV curves for both the fabricated and simulated devices. Minor discrepancies can be observed between the performance parameters of the fabricated and simulated devices. However, these discrepancies fall within the acceptable performance range of the fabricated device. This is evident when comparing samples A1, A2, and A3 with the simulated fabricated device, as detailed in Table 4. Additionally, Figure 10 compares the simulated fabricated device with the simulated optimized device. The simulated fabricated device corresponds to the fabricated A3 sample, while the simulated

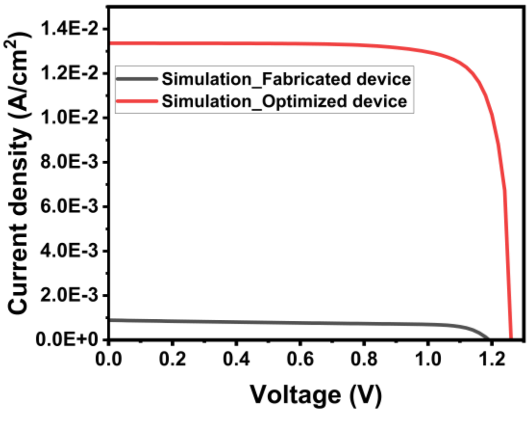

Fig 10. Simulation IV curve for fabricated and optimized $Cs_3Bi_2I_9$ solar cell.

Table 4
Comparison between fabricated and S-Q limit solar cell performance based on optical bandgap.

Sample	Bandgap (eV)	J_{SC} (mA/cm^2)	V_{OC} (V)	FF	Eff. (%)
A1	1.9	0.87	0.90	71	0.61
A2	2.1	0.93	1.25	49	0.54
A3	2.0	0.81	1.1	78	0.72
S-Q1	1.9	16.97	1.58	91.8	24.75
S-Q2	2.1	12.48	1.78	92.5	20.50
S-Q3	2.0	14.59	1.68	92.2	22.62
Simulation fabricated device	2.0	0.88	1.19	66	0.70
Simulation optimized device	2.0	13.36	1.27	80.73	13.75

optimized device represents the optimized version of the A3 device. A notable increase in the short-circuit current density (J_{SC}) from 0.88 mA/cm^2 to 13.38 mA/cm^2 results in a significant improvement in efficiency, which can reach up to 13.75%. This improvement is primarily attributed to enhancements in the minority carrier lifetime and thickness of the absorber layer. By optimizing the bulk defect density and improving the minority carrier lifetime in the film, a lifetime of 1 ns can be achieved, a value that has also been reported in other literature. A higher minority carrier lifetime indicates that carriers can remain in the conduction band for a longer period, thereby increasing the likelihood of more carriers reaching the terminal, which ultimately improves device performance (Sepeai *et al.*, 2017; Zulhafizhazuan *et al.*, 2017).

6. Conclusion

In conclusion, the analysis of the fabricated FTO/TiO_2/$Cs_3Bi_2I_9$/Spiro-OmeAtad/Ag solar cells reveal that sample A3 exhibits superior performance, achieving a 0.72% efficiency improvement compared to the other samples. This enhanced performance is primarily attributed to A3's superior optoelectronic properties, including larger crystallite size, lower strain, and minimal dislocation density, which collectively reduce recombination losses and enhance carrier mobility. The high absorption rate and longer carrier lifetime in A3 further contribute to its effectiveness in converting light to electricity, bringing it closer to the theoretical S-Q limit.

The study highlights the crucial role of material quality in photovoltaic performance, particularly the relationship between carrier lifetime, diffusion length, and film thickness. As demonstrated, a balance between these factors is essential for achieving efficient charge collection and minimizing recombination losses. The SCAPS-1D simulation results corroborate the experimental findings, showing that by optimizing material parameters such as minority carrier lifetime and absorber layer thickness, the efficiency of the solar cell can be significantly improved.

These findings underscore the importance of precise material engineering in the development of high-efficiency solar cells. Future work should focus on further refining these parameters and exploring additional optimization techniques to push the efficiency of $Cs_3Bi_2I_9$ solar cells closer to their theoretical limits. The success of sample A3 provides a promising direction for future research and development in the field of photovoltaics.

Acknowledgments

The authors gratefully acknowledge the Ministry of Higher Education, Malaysia, and MIMOS BHD for their support through research grant RS-2021-003. The authors also extend their appreciation to Marc Burgelman and his colleagues at the University of Gent for developing the SCAPS-1D program, which was used for all simulations in this work.

Author Contributions: Wan Zulhafizhazuan: Conceptualization, methodology, formal analysis, writing—original draft, Md Khan Sobayel Bin Rafiq; Conceptualization Data Curation, Software, Validation, Review & Editing, Supervision. Shafidah Safian; Review & Editing. Suhaila Sepeai; Project Administration, Validation. Mohd Adib Ibrahim; Project Administration, Validation, Funding Acquisition. All authors have read and agreed to the published version of the manuscript.

Funding: The authors fully acknowledge the contribution of the Ministry of Higher Education, Malaysia and MIMOS BHD for the research grant RS-2021-003.

Conflicts of Interest: The authors declare no conflict of interest.

References

Ahamd, F., Lakhtakia, A., & Monk, P. B. (2020). *Double-absorber thin-film solar cell with 34% efficiency*; https://doi.org/10.1063/5.0017916

Ahmed, S., Akhtaruzzaman, M., Zulhafizhazuan, W., Yusoff, Y., Alnaser, I. A., Karim, M. R., Shahiduzzaman, M., & Sobayel, K. (2023). Theoretical verification of using the Ga-doped ZnO as a charge transport layer in an inorganic perovskite solar cell. *Japanese Journal of Applied Physics*, *62*(9).https://doi.org/10.35848/1347-4065/ACED74

Akhtaruzzaman, M., Shahiduzzaman, M., Amin, N., Muhammad, G., Islam, M. A., Sobayel Bin Rafiq, K., & Sopian, K. (2021). Impact of Ar flow rates on micro-structural properties of WS_2 thin film by rf magnetron sputtering. *Nanomaterials*, *11*(7). https://doi.org/10.3390/nano11071635

Aliaghayee, M. (2023). Optimization of the Perovskite Solar Cell Design with Layer Thickness Engineering for Improving the Photovoltaic Response Using SCAPS-1D. *Journal of Electronic Materials*, *52*(4), 2475–2491.https://doi.org/10.1007/S11664-022-10203-X/METRICS

Bai, F., Hu, Y., Hu, Y., Qiu, T., Miao, X., & Zhang, S. (2018). Lead-free, air-stable ultrathin $Cs_3Bi_2I_9$ perovskite nanosheets for solar cells. *Solar Energy Materials and Solar Cells*, *184*, 15–21. https://doi.org/10.1016/j.solmat.2018.04.032

Basher, M. K., Alam, M. N. E., & Alameh, K. (2021). Design, Development, and Characterization of Low Distortion Advanced Semitransparent Photovoltaic Glass for Buildings Applications. *Energies 2021, Vol. 14, Page 3929*, *14*(13), 3929. https://doi.org/10.3390/EN14133929

Bragg H.W., B.L.W. (1913). *Proceedings of the Royal Society of London. Series A, Containing Papers of a Mathematical and Physical Character*, *88*(605), 428–438. https://doi.org/10.1098/rspa.1913.0040

Cheng, H., Feng, Y., Fu, Y., Zheng, Y., Shao, Y., & Bai, Y. (2022). Understanding and minimizing non-radiative recombination losses in perovskite light-emitting diodes. *Journal of Materials Chemistry C*, *10*(37), 13590–13610. https://doi.org/10.1039/D2TC01869A

Debby Coa (2024) *Is Perovskite the Future of Solar Energy?* https://www.solarctrl.com/blog/is-perovskite-the-future-of-solar-energy/ Accessed on 14 August 2024

Feierabend, M., Morlet, A., Berghäuser, G., & Malic, E. (2017). Impact of strain on the optical fingerprint of monolayer transition-metal dichalcogenides. *Physical Review B*, *96*(4), 045425. https://doi.org/10.1103/PHYSREVB.96.045425/FIGURES/5/MEDIUM

Ghosh, B., Wu, B., Mulmudi, H. K., Guet, C., Weber, K., Sum, T. C., Mhaisalkar, S., & Mathews, N. (2018). Limitations of $Cs_3Bi_2I_9$ as Lead-Free Photovoltaic Absorber Materials. *ACS Applied Materials and Interfaces*, *10*(41), 35000–35007. https://doi.org/10.1021/acsami.7b14735

Hamukwaya, S. L., Hao, H., Mashingaidze, M. M., Zhong, T., Tang, S., Dong, J., Xing, J., & Liu, H. (2022). Potassium Iodide-Modified Lead-Free $Cs_3Bi_2I_9$ Perovskites for Enhanced High-Efficiency Solar Cells. *Nanomaterials*, *12*(21). https://doi.org/10.3390/nano12213751

Han, H., Park, J., Nam, S. Y., Kim, K. J., Choi, G. M., Parkin, S. S. P., Jang, H. M., & Irvine, J. T. S. (2019). Lattice strain-enhanced exsolution of nanoparticles in thin films. *Nature Communications*, *10*(1). https://doi.org/10.1038/S41467-019-09395-4

Hartono, N. T. P., Sun, S., Gélvez-Rueda, M. C., Pierone, P. J., Erodici, M. P., Yoo, J., Wei, F., Bawendi, M., Grozema, F. C., Sher, M. J., Buonassisi, T., & Correa-Baena, J. P. (2019). The effect of structural dimensionality on carrier mobility in lead-halide perovskites. *Journal of Materials Chemistry A*, *7*(41), 23949–23957. https://doi.org/10.1039/c9ta05241k

Iftekharuzzaman, I., Ghosh, S., Basher, M. K., Islam, M. A., Das, N., & Nur-E-Alam, M. (2023). Design and Concept of Renewable Energy Driven Auto-Detectable Railway Level Crossing Systems in Bangladesh. *Future Transportation*, *3*(1), 75–91. https://doi.org/10.3390/FUTURETRANSP3010005/S1

Islam, M. A., Rafiq, M. K. S. Bin, Misran, H., Uzzaman, M. A., Techato, K., Muhammad, G., & Amin, N. (2020). Tailoring of the Structural and Optoelectronic Properties of Zinc-Tin-Oxide Thin Films via Oxygenation Process for Solar Cell Application. *IEEE Access*, *8*, 193560–193568. https://doi.org/10.1109/ACCESS.2020.3031894

Islam, M. B., Yanagida, M., Shirai, Y., Nabetani, Y., & Miyano, K. (2017). NiO_x Hole Transport Layer for Perovskite Solar Cells with Improved Stability and Reproducibility. *ACS Omega*, *2*(5), 2291–2299. https://doi.org/10.1021/acsomega.7b00538

Johansson, M. B., Philippe, B., Banerjee, A., Phuyal, D., Mukherjee, S., Chakraborty, S., Cameau, M., Zhu, H., Ahuja, R., Boschloo, G., Rensmo, H., & Johansson, E. M. J. (2019). Cesium Bismuth Iodide Solar Cells from Systematic Molar Ratio Variation of CsI and BiI_3. *Inorganic Chemistry*, *58*(18), 12040–12052. https://doi.org/10.1021/acs.inorgchem.9b01233

Johansson, M. B., Zhu, H., & Johansson, E. M. J. (2016). Extended Photo-Conversion Spectrum in Low-Toxic Bismuth Halide Perovskite Solar Cells. *Journal of Physical Chemistry Letters*, *7*(17), 3467–3471. https://doi.org/10.1021/acs.jpclett.6b01452

Jung, E. H., Jeon, N. J., Park, E. Y., Moon, C. S., Shin, T. J., Yang, T. Y., Noh, J. H., & Seo, J. (2019). Efficient, stable and scalable perovskite solar cells using poly(3-hexylthiophene). *Nature 2019 567:7749*, *567*(7749), 511–515. https://doi.org/10.1038/s41586-019-1036-3

Li, S., Cao, Y. L., Li, W. H., & Bo, Z. S. (2021). A brief review of hole transporting materials commonly used in perovskite solar cells. *Rare Metals*, *40*(10), 2712–2729. https://doi.org/10.1007/S12598-020-01691-Z

Lian, J., Lu, B., Niu, F., Zeng, P., & Zhan, X. (2018). Electron-Transport Materials in Perovskite Solar Cells. In *Small Methods* (Vol. 2, Issue 10). John Wiley and Sons Inc. https://doi.org/10.1002/smtd.201800082

Liou, J. C., Diao, C. C., Lin, J. J., Chen, Y. L., & Yang, C. F. (2014). Prepare dispersed CIS nano-scale particles and spray coating CIS absorber layers using nano-scale precursors. *Nanoscale Research Letters*, *9*(1), 1. https://doi.org/10.1186/1556-276X-9-1

Max-Planck-Gesellschaft.(2024) https://www.mpg.de/8431287/efficiency_perovskite-solar-cell Accessed 14 August 2024

McGovern, L., Koschany, I., Grimaldi, G., Muscarella, L. A., & Ehrler, B. (2021). Grain Size Influences Activation Energy and Migration Pathways in MAPbBr3Perovskite Solar Cells. *Journal of Physical Chemistry Letters*, *12*(9), 2423–2428. https://doi.org/10.1021/ACS.JPCLETT.1C00205/SUPPL_FILE/JZ1C00205_SI_001.PDF

Mohamad Noh, M. F., Teh, C. H., Daik, R., Lim, E. L., Yap, C. C., Ibrahim, M. A., Ahmad Ludin, N., Mohd Yusoff, A. R. Bin, Jang, J., & Mat Teridi, M. A. (2018). The architecture of the electron transport layer for a perovskite solar cell. In *Journal of Materials Chemistry C* (Vol. 6, Issue 4, pp. 682–712). Royal Society of Chemistry. https://doi.org/10.1039/c7tc04649a

Morales, M., & Al-Shomar, S. M. (2024). Influence of Post-Annealing Treatment on Some Physical Properties of Cerium Oxide Thin Films Prepared by the Sol–Gel Method. *Crystals 2024, Vol. 14, Page 615*, *14*(7), 615. https://doi.org/10.3390/CRYST14070615

Mosabbir, A. S. M., Sadek, M. S., Mahmood, M., Mofazzal Hosain, M., Sepeai, S., Chelvanathan, P., Sultan, S. M., Sopian, K., Ibrahim, M. A., & Sobayel, K. (2024). Optimizing lead-free Cs2AgBiBr6 double perovskite solar cells: insights from SCAPS and FDTD simulations. *Sustainable Energy & Fuels*, *8*(18), 4311–4323. https://doi.org/10.1039/D4SE00958D

Namatame, M., Yabusaki, M., Watanabe, T., Ogomi, Y., Hayase, S., & Marumoto, K. (2017). Direct observation of dramatically enhanced hole formation in a perovskite-solar-cell material spiro-OMeTAD by Li-TFSI doping. *Applied Physics Letters*, *110*(12). https://doi.org/10.1063/1.4977789

Ng, H. K., Xiang, D., Suwardi, A., Hu, G., Yang, K., Zhao, Y., Liu, T., Cao, Z., Liu, H., Li, S., Cao, J., Zhu, Q., Dong, Z., Tan, C. K. I., Chi, D., Qiu, C. W., Hippalgaonkar, K., Eda, G., Yang, M., & Wu, J. (2022). Improving carrier mobility in two-dimensional semiconductors with rippled materials. *Nature Electronics 2022 5:8*, *5*(8), 489–496. https://doi.org/10.1038/s41928-022-00777-z

Nur-E-Alam, M., Islam, M. A., Kar, Y. B., Kiong, T. S., Misran, H., Khandaker, M. U., Fouad, Y., Soudagar, M. E. M., & Cuce, E. (2024). Anti-solvent materials enhanced structural and optical properties on ambiently fabricated perovskite thin films. *Scientific Reports 2024 14:1, 14(1), 1–11.* https://doi.org/10.1038/s41598-024-70344-3

Nur-E-Alam, M., Zehad Mostofa, K., Kar Yap, B., Khairul Basher, M., Aminul Islam, M., Vasiliev, M., Soudagar, M. E. M., Das, N., & Sieh Kiong, T. (2024). Machine learning-enhanced all-photovoltaic blended systems for energy-efficient sustainable buildings. *Sustainable Energy Technologies and Assessments, 62, 103636.* https://doi.org/10.1016/J.SETA.2024.103636

NREL (2024) https://www.nrel.gov/pv/cell-efficiency.html. Accessed 14 August 2024

O, S., G, A., & O, D. (2016). Simulation of the Performance of CdTe/CdS/ZnO Multi- Junction Thin Film Solar Cell. *Review of Information Engineering and Applications*, *3*(1), 1–10. https://doi.org/10.18488/journal.79/2016.3.1/79.1.1.10

Rai, N., Rai, S., Singh, P. K., Lohia, P., & Dwivedi, D. K. (2020). Analysis of various ETL materials for an efficient perovskite solar cell by numerical simulation. *Journal of Materials Science: Materials in Electronics*, *31*(19), 16269–16280. https://doi.org/10.1007/s10854-020-04175-z

Ramli, N. F., Sepeai, S., Rostan, N. F. M., Ludin, N. A., Ibrahim, M. A., Teridi, M. A. M., & Zaidi, S. H. (2017). Model development of monolithic tandem silicon-perovskite solar cell by SCAPS simulation. *AIP Conference Proceedings, 1838.* https://doi.org/10.1063/1.4982178

Razza, S., Castro-Hermosa, S., Di Carlo, A., & Brown, T. M. (2016). Research Update: Large-area deposition, coating, printing, and processing techniques for the upscaling of perovskite solar cell technology. *APL Materials*, *4*(91508), 091508. https://doi.org/10.1063/1.4962478

Rühle, S. (2016). Tabulated values of the Shockley-Queisser limit for single junction solar cells. Solar Energy, 130, 139–147. https://doi.org/10.1016/j.solener.2016.02.015

Sarkar, P., Niranjan, N. K., Srivastava, A., Tripathy, S. K., Baishnab, K. L., & Chinnaiah, M. C. (2022). Comparative Study on the Role of Different Precursor Salts on Structural, Morphological, and Optoelectronic Characteristics of CH_3NH3PbCl3 Perovskite Semiconductor: An Experimental Study. *Journal of Electronic Materials*, *51*(12), 7105–7112. https://doi.org/10.1007/S11664-022-09946-4/METRICS

Sepeai, S., Zulhafizhazuan, W., Leong, C. S., Ludin, N. A., Ibrahim, M. A., Sopian, K., & Zaidi, S. H. (2017). Analisis arus-voltan bagi pengubahsuaian proses fabrikasi sel suria silikon jenis-P ke atas wafer silikon jenis-N. *Sains Malaysiana*, *46*(10), 1943–1949. https://doi.org/10.17576/jsm-2017-4610-33

Thomas Ovenden (2024*) The Environmental Impact of Fossil Fuels vs. Renewable Energy: Making the Switch for a Healthier* https://www.nfuenergy.co.uk/news/environmental-impact-fossil-fuels-vs-renewable-energy-making-switch-healthier-planet Accessed on 14 August 2024

Waykar, R., Bhorde, A., Nair, S., Pandharkar, S., Gabhale, B., Aher, R., Rondiya, S., Waghmare, A., Doiphode, V., Punde, A., Vairale, P., Prasad, M., & Jadkar, S. (2020). Environmentally stable lead-free cesium bismuth iodide ($Cs_3Bi_2I_9$) perovskite: Synthesis to solar cell application. *Journal of Physics and Chemistry of Solids*, *146*, 109608. https://doi.org/10.1016/J.JPCS.2020.109608

Yadav, S., Gupta, S. K., & Negi, C. M. S. (2024). Comprehensive Analysis of Lead-Free Perovskite (CsSn0.5Ge0.5I3) Solar Cell: Impact of Active Layer Thickness and Defect Density. *Brazilian Journal of Physics*, *54*(3), 1–9. https://doi.org/10.1007/S13538-024-01444-8/METRICS

Yao, W., Hu, S., Jia, F., Reimers, J. R., Wang, Y., Singh, D. J., & Ren, W. (2022). Lattice strain and band overlap of the thermoelectric composite Mg2Si1-xSnx. *Physical Review B*, *106*(10), 104303. https://doi.org/10.1103/PHYSREVB.106.104303/FIGURES/4/MEDIUM

Yin, X., Guo, Y., Xie, H., Que, W., & Kong, L. B. (2019). Nickel Oxide as Efficient Hole Transport Materials for Perovskite Solar Cells. In *Solar RRL* (Vol. 3, Issue 5). Wiley-VCH Verlag. https://doi.org/10.1002/solr.201900001

Yu, Y., Xia, J., & Liang, Y. (2022). Basic understanding of perovskite solar cells and passivation mechanism. *AIP Advances*, *12*(5), 55307. https://doi.org/10.1063/5.0058441/2819457

Yun, A. J., Kim, J., Hwang, T., & Park, B. (2019). Origins of Efficient Perovskite Solar Cells with Low-Temperature Processed SnO2 Electron Transport Layer. *ACS Applied Energy Materials*, *2*(5), 3554–3560. https://doi.org/10.1021/ACSAEM.9B00293

Zhang, L., Mao, H., Huang, L., Hu, L., Wang, X., Tan, L., & Chen, Y. (2022). Achieving improved stability and minimal non-radiative recombination loss for over 18% binary organic photovoltaics via versatile interfacial regulation strategy. *Science China Chemistry*, *65*(8), 1623–1633. https://doi.org/10.1007/S11426-022-1300-1/METRICS

Zhang, L., Wang, K., & Zou, B. (2019). Bismuth Halide Perovskite-Like Materials: Current Opportunities and Challenges. *ChemSusChem*, *12*(8), 1612–1630. https://doi.org/10.1002/cssc.201802930

Zhou, X., Wang, T., Liang, X., Wang, F., Xu, Y., Lin, H., Hu, R., & Hu, H. (2023). Long-chain organic molecules enable mixed dimensional perovskite photovoltaics: a brief view. *Frontiers in Chemistry*, *11*. https://doi.org/10.3389/FCHEM.2023.1341935

Zulhafizhazuan, W., Sepeai, S., Leong, C. S., Sopian, K., & Zaidi, S. H. (2017). Analisis prestasi bagi sel suria silikon teringkas ke atas silikon wafer kristal jenis-P. *Malaysian Journal of Analytical Sciences*, *21*(5), 1127–1133. https://doi.org/10.17576/mjas-2017-2105-15